

Accelerated discovery of solid-state electrolytes using Bayesian optimisation

Sherif Abdulkader Tawfik,¹ Julian Berk,¹ Tiffany Walsh,² Santu Rana,¹ Svetha Venkatesh¹

¹*Applied Artificial Intelligence Institute, Deakin University, Geelong, Victoria 3216, Australia*

²*Institute for Frontier Materials, Deakin University, Geelong, Victoria 3216, Australia*

Abstract

Current lithium batteries do not fully meet the longevity and safety requirements of electric vehicles. Novel solid state lithium ion batteries could be a compelling solution to these problems. In this work we unravel some of these new materials with potentially high lithium conductivity by using a Bayesian optimization approach. This involves exploring the material space for new solid-state electrolyte materials with the objective of maximising - lithium diffusivity. The materials selected by the Bayesian optimisation algorithm are then examined using *ab initio* molecular dynamics to estimate their diffusion energy barrier. We establish that the materials are electronic insulators, a requirement in electrolyte materials, by computing the electronic bandgaps of each of the selected materials using a hybrid exchange method, and then examine the stability of the materials at the lithium metal anode interface by computing the crystal decomposition energies. Out of the selected materials, we find that Li₃YBr₆ has a reasonably low diffusion barrier, a high bandgap and is potentially the most stable material at the lithium metal interface. In addition to introducing stable and high-diffusivity solid-state electrolyte materials, our work presents a material discovery method that can be applied for a broad range of applications.

1. Introduction

The increasing demand for electric vehicles (EV) and portable electronics is fuelling the pressure to manufacture millions of rechargeable lithium-ion batteries (LIBs) yearly. According to International Energy Agency, 6.6 million electric vehicles were sold globally in 2021.¹ EVs require batteries that: minimize risk to the lives of passengers, have large energy capacity for longer driving range, and can perform under a range of environmental conditions. Although state-of-the-art commercial LIB technologies have demonstrated the ability to fulfill these requirements, they have many limitations: they suffer from degradation and are at risk of explosion due to short-circuiting.² Research in Solid-state lithium-ion batteries are rising to the forefront as a replacement to current LIBs.² Importantly, major car manufacturers, including Toyota, BMW and Ford, have started investing - the development of solid-state LIBs for their vehicles: the first test EV battery models are projected to launch in 2024.³

In solid-state LIBs, the electrolyte is solid (solid-state electrolyte, SSE) rather than a liquid, and therefore is less susceptible to dendrite formation (for which the risk is reduced but not eliminated completely), and less sensitive to temperature changes- and - to explosion. Importantly, the reported energy densities of SSELs are capable of satisfying the energy needs of EVs while ensuring lower battery volume and longer driving range.²

Recent momentum towards the commercialisation of these batteries has been driving the search for efficient means to discover new solid-state battery materials. Theoreticians and experimentalists alike have been able to discover many materials as candidates for solid-state

LIBs. While theoreticians have benefitted from the near-negligible cost of material exploration, the need to synthesise new battery materials can make materials exploration prohibitively expensive for experimentalists. The principal theoretical approach for modelling SSEL materials – density functional theory (DFT), has been particularly successful in accurately predicting key SSEL parameters such as the electronic bandgap and the diffusion coefficients.⁴ Compounded with high-throughput screening workflows^{5,6} and applying machine learning,⁵ thousands of candidate materials have been examined, from which new materials have been proposed. Although several solid-state electrolytes have been discovered over the last decades with high theoretical capacity, solid-state batteries have not yet been commercialised because of their critical limitations, particularly lower lithium conductivity than the liquid counterparts, and the fact that complex chemistries at the electrode/electrolyte interface compromise the conductivity and the overall battery capacity (known as *capacity fade*). High diffusivity SSE materials such as LGPS, fail to sustain their conductivity due to the crystal decomposition of the material at the lithium metal|SSE interface. Therefore, the discovery of new SSEL materials is a critical requirement for the evolution of all-solid-state batteries towards commercialisation.

With the increasingly massive space of candidate SSE materials available in online databases, it is becoming hypothetically possible to discover new SSEL materials for Li batteries, when a high-throughput screening procedure is combined with machine learning. One can, in principle, also generate new hypothetical materials and apply machine learning to rapidly identify materials that can be potentially synthesized. However, a critical problem in SSE research is the scarcity of the relevant data, as was emphasized in Ref. ⁷: even though the databases provide structural and key energetic properties, they lack critical information on the performance of the materials as lithium diffusion materials. This scarcity is due to the high cost involved in performing a calculation of the ion diffusion coefficients for SSEL materials.

In this work, we address this data scarcity challenge by introducing a novel material discovery approach using Bayesian Optimisation (BO). BO is a highly sample efficient optimization algorithm that can optimize expensive black-box systems.⁸ Here, the term “sample efficient” means that the algorithm can work with limited data, making it a natural fit for optimizing simulations with high computational cost such as the simulations presented in Refs^{9,10}.

2. Computational details

Dataset We compile a dataset of 98 materials along with their diffusion coefficients at 1000 K using 96 samples obtained from the work of Kahle et al.⁶ and 2 samples from our calculations. Each structure in the dataset is downloaded from its respective database repository (COD and ICSD). The value of the diffusion coefficient at a high temperature is an indication of the diffusivity of the material, and we use the temperature of 1000 K as was used in Ref⁶. The lithium diffusion coefficients were computed Ref⁶ using the plane-wave code Quantum Espresso, whereas this work computes the diffusion coefficients using plane-wave code VASP. This dataset is used for training the Gaussian process model in the Bayesian optimization algorithm, which is described in the following section.

Bayesian optimization This approach works by generating a Gaussian process surrogate model of the system using existing data. The Gaussian process is used because it gives predictions for both the model outputs themselves along with - uncertainties about the predictions. This allows us to select new materials to simulate based both on how much they are predicted to improve over the best current solutions as well as how much they improve

the Gaussian process by reducing its epistemic uncertainty. The result from these simulations is then added to training data, allowing for an improved Gaussian process modelling and for a new set of suggestions to be obtained. This is iterated until the desired solution is obtained or until the experimental budget has been exhausted.

It is assumed that the measured diffusivities are corrupted by some random, normally distributed noise $\epsilon_n \sim N(0, \sigma_n)$. This means that, for a given input x , we observe $y = f(x) + \epsilon_n$ instead of the “true” log diffusivities $f(x)$. These input-output pairs give us an initial dataset with which to train our first Gaussian process model.

Gaussian process: The Gaussian process maps each input from our search space to a Gaussian random variable: $f'(x) \sim GP(m(x), k(x, x'))$. It is characterised by a prior mean function $m(x)$ and a kernel (aka covariance function) $k(x, x')$. As we do not know a prior mean function, we simply standardise the log diffusivities and use a prior mean of $m(x) = 0$. In this case, we chose to use the sum of two kernels $k(x_i, x_j) = w_1 k_1(x_i, x_j) + w_2 k_2(x_i, x_j)$. We set the first as the square exponential kernel

$$k_1(x_i, x_j) = \exp\left(-\frac{\|x_i - x_j\|^2}{2l^2}\right)$$

As this is a function of the distance between points, it makes nearby points highly correlated. This results in smooth, well-behaved predictions. However, this does not allow for global trends to be captured by our kernel. For this, we add a dot product kernel

$$k_2(x_i, x_j) = x_i \cdot x_j$$

This means that our Gaussian process has a length scale parameter, l , two weight parameters, w_1 and w_2 , and the noise level parameter σ_n . As the Gaussian process is a statistical model, all of these can be fit with maximum likelihood during the models training.

Once trained, the Gaussian process gives a predictive distribution as a Gaussian distribution for each material:

$$f'(x) \sim N(\mu(x), \sigma(x))$$

Acquisition function: Once we have the Gaussian process, we need to use it to suggest new samples. This is done by using an acquisition function $\alpha(x)$ to optimally balance suggesting samples which are predicted to have high log diffusivities, and samples which better improve the Gaussian Process model to allow for better future predictions. A common and efficient acquisition function is expected improvement. This simply encodes the expected amount of improvement a material will give over the current best-found material $f(x^+)$ [1]:

$$\begin{aligned} I(x) &= \max \{0, f'(x) - f(x^+)\} \\ \alpha(x) &= \mathbb{E}(I(x)) = \begin{cases} (\mu(x) - f(x^+))\Phi(Z) + \sigma(x)\phi(Z) & \text{if } \sigma(x) > 0 \\ 0 & \text{if } \sigma(x) = 0 \end{cases} \end{aligned}$$

Where $Z = (\mu(x) - f(x^+))/\sigma(x)$, Φ is the standard normal CDF and ϕ is the standard normal PDF.

With this, the next sample is simply the material that gives the highest acquisition function value.

$$x' = \arg \max_{x \in X} \alpha(x) \quad (1)$$

Where X is the search space containing a list of candidate materials. As we have a finite number of candidate materials and the acquisition function is cheap to compute, we can find the above by simply evaluating the acquisition function for all potential materials. We display a schematic illustration of the BO procedure we apply in this work.

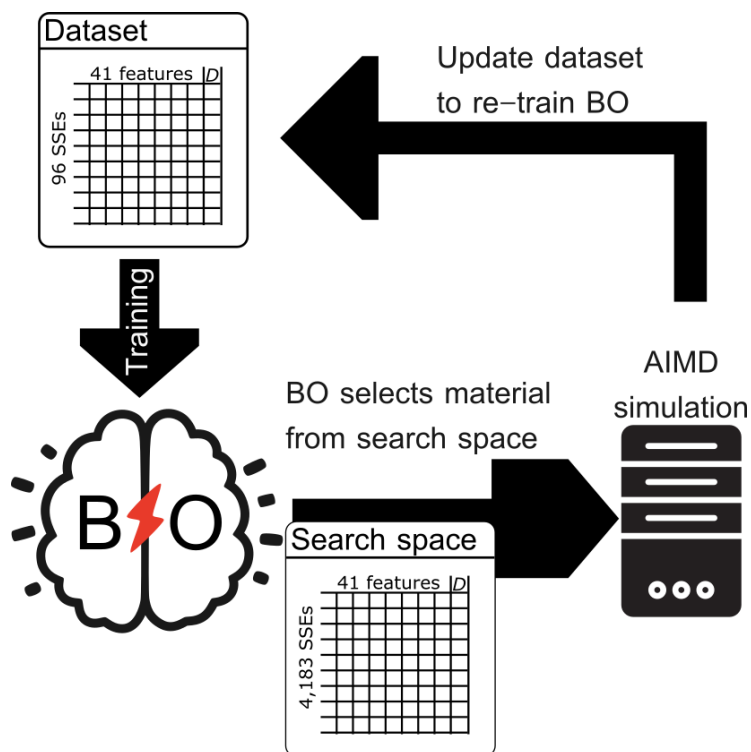


Figure 1: A schematic illustration of the BO solid state electrolyte (SSE) discovery loop. The initial training dataset has 96 SSE materials, where the data D (the values of the diffusion coefficients at 1000 K) was obtained from Kahle et al.⁶ We train the BO algorithm on this dataset, and then iteratively let the algorithm suggest SSE materials from the search space. For each suggested material, we perform AIMD simulations in order to obtain the diffusion coefficient of Lithium at 1000 K. We then incorporate this new data point into the training set, and re-train the BO algorithm.

Featurization Each structure is represented to the GP in terms of the relationships between the Li, cation and anion sites within the crystal structure while considering the crystal periodicity. We have utilized 41 features including features adapted from Ref. ⁵, and features that we have explained in Section S1 of the Supplementary Information.

Search space The BO algorithm searches for candidate materials in a space of 4,183 materials, which is our search space. The materials in the search space were retrieved from the Materials Project¹¹ (MP) database using the python library pymatgen, and the search query had the following conditions: the material must include Li, a bandgap > 1 eV, and the energy above the convex hull < 50 meV. The last condition is indicative of the thermodynamic stability of the retrieved material.

AIMD simulations These were performed using the Vienna *Ab initio* Simulation Package (VASP),¹² within the generalized gradient approximation functional with the PBE parametrization. The calculations were performed with an energy cut-off of 450 eV at the Γ -

point, and with no spin-polarization. The Nose-Hoover thermostat was applied, and a time step of 1 fs was used for all of the AIMD simulations. For generating the dataset for training the BO algorithm, the temperature applied for all simulations was 1000 K.

The diffusion coefficient for each species at a given temperature T was calculated based on the formula

$$D = \frac{\text{MSD}}{2dt} \quad (2)$$

where d is the dimensionality of the calculation ($d = 3$ corresponds to diffusion in all dimensions in a bulk crystal), t is the time, and the mean square displacement, MSD, is given by

$$\text{MSD} = \frac{1}{N} \sum_{i=1}^N \langle [\mathbf{r}_i(t + t_0) - \mathbf{r}_i(t_0)]^2 \rangle \quad (3)$$

where N is the total number of the species in the supercell, $\mathbf{r}_i(t)$ is the position of atom i at time t during the simulation, and the operation $\langle \dots \rangle$ is an ensemble average.

A known challenge⁶ in the simulation of ionic diffusion in crystal structures using AIMD is the restriction on the size of the simulation cell due to the high computational cost of AIMD simulations of structures that include heavy atoms. This size restriction affects the quality of the generated trajectories. In order to achieve a computational cost vs. quality trade-off, we run AIMD simulations at 1000 K for relatively short periods of time (around 30 ps) to obtain the diffusion coefficients for the materials suggested by the BO acquisition function. After the conclusion of the BO iterations, we run AIMD simulations for similar time periods but covering a broad range of temperatures from 600 K up to 1,300 K to compute an estimate for the diffusion barrier. The diffusion barrier is then obtained from the slope m of the Arrhenius plot, which is the \log_{10} of the diffusion coefficient versus in the inverse of the temperature:

$$E_A = -1000k_B m \quad (4)$$

Another challenge in this type of simulations is that the diffusion coefficients obtained from simulations conducted at various temperatures might not align along the Arrhenius plot, in addition to suffering from high errors. There are several examples of such materials that were presented in the supplementary information of Ref. ⁶, such as RbLi₇Si₂O₈ (ICSD 33864), Li₂S₂O₇ (ICSD 188009) and Li₂ZnSnSe₄ (COS 7035178). This is in spite of the long simulation times reported in this work, which exceeded 0.2 ns in many cases. This situation makes it difficult to obtain a clear picture for the diffusivity at room temperature for many materials, and therefore the conclusions that can be drawn from the AIMD simulations are mainly qualitative. We overcome this challenge by aligning as many points as possible on the Arrhenius plot within the range of temperatures considered in this work.

DFT calculations For each of the materials with the highest $D_{1000\text{K}}$ values, we calculate the electronic bandgap and the thermodynamical stability. The electronic structure is calculated in a single point calculation using the hybrid exchange HSE method to obtain an accurate estimate for the bandgaps. A critical aspect of SSE stability is to examine its thermodynamic stability at the lithium metal interface. This can be done by the introduction of excess Li atoms, similar to the procedure in Ref. ¹². Our calculations of the crystal decomposition are based on the crystal energies reported in the MP database at zero electrostatic potential (that is, we take $\varphi = 0$ in Eq. 1 of Ref. ¹³).

The defect formation energy E^f for a structure as a function of the Fermi energy E_F is given by the formula

$$E^f(E_F) = E_{tot}[q] - (E_{bulk} + \sum_{i=1}^N \mu_i n_i) + q E_F \quad (5)$$

where q is the charge state of the defect, $E_{tot}[q]$ is the total energy of the defect supercell that is optimised at charge state q , E_{bulk} is the total energy of the bulk supercell which has the same size as that of the defect supercell.

3. Results and discussion

3.1 Selections made by the BO algorithm

The BO algorithm is run iteratively to suggest materials from the search space. For each of the suggested structures, we compute D_{1000K} using AIMD. We adopted a threshold value for the diffusion coefficient of $2 \times 10^{-5} \text{ cm}^2/\text{s}$, below which a material selected by the acquisition function will be considered to have low conductivity. We have run the BO algorithm for 14 iterations and obtained the 38 suggestions, of which we found 7 materials with D_{1000K} values exceeding the threshold value. We display the diffusivities of these materials in Figure 2.

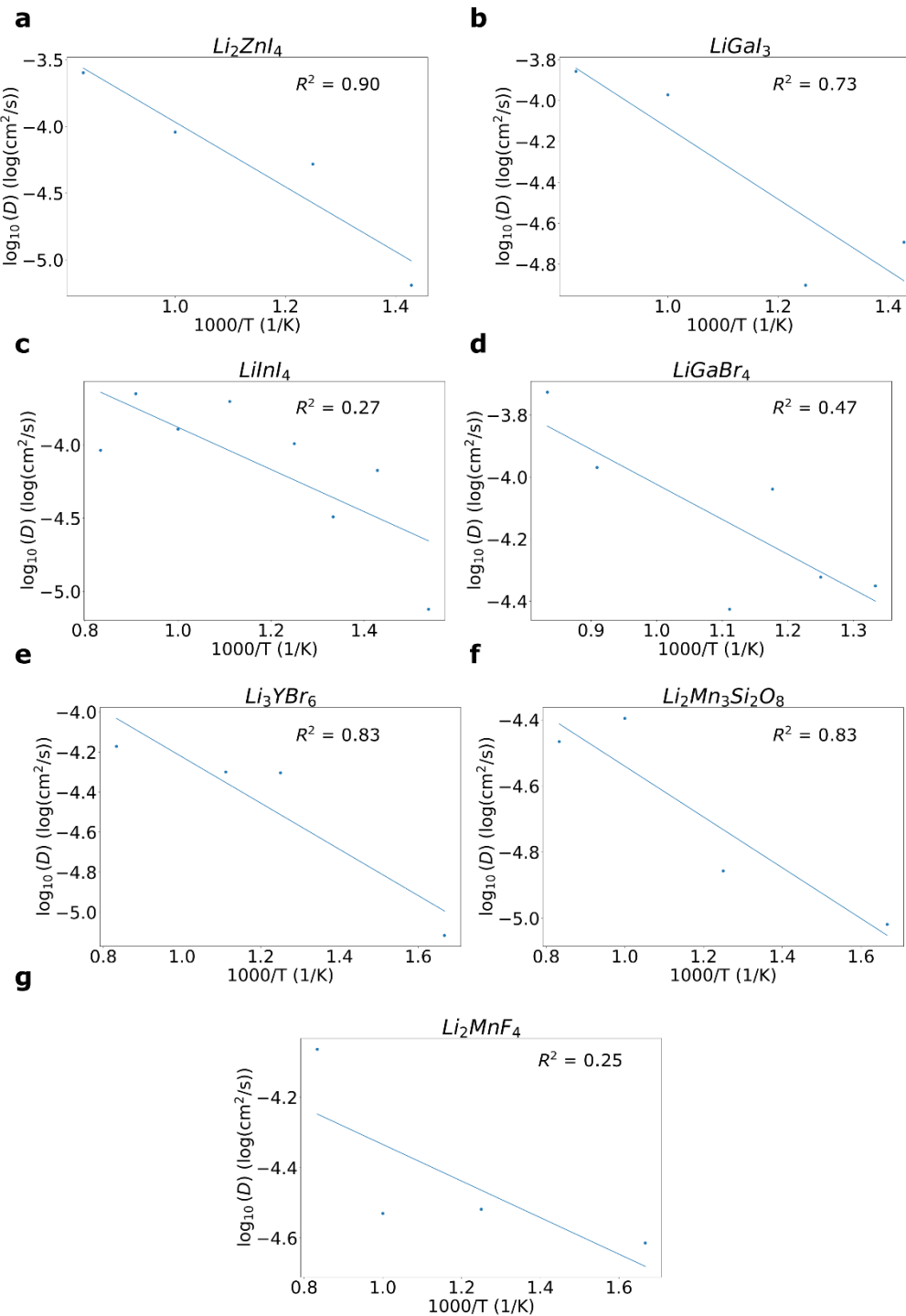


Figure 2: Arrhenius plot for the top 7 materials suggested by the BO acquisition function. The R^2 for the goodness of fit is displayed within each plot.

The BO algorithm commences by exploiting its learned knowledge of halide materials in the dataset, suggesting lithium metal halides - are related to several of the highest diffusivity materials in Ref. 6.

Li₂ZnI₄ (mp-23497): This ternary lithium halide belongs to the family of highly conductive compounds Li_2MX_4 ($M = Mg, V, Cr, Mn, Co, Cd, X = Cl, Br, I$)¹⁴ and its synthesised was reported by Pfitzner et al. in 1990.¹⁴ The energy above the convex hull for this material is 27 meV/atom and is therefore potentially stable. The crystal structure is orthorhombic with the

space group *Pnma*, where iodine ions form a hexagonal framework, and the Li and Zn ions occupy octahedral voids. The lithium conductivity of the chloride structure is 3×10^{-4} S/cm at 300 K, which is one of the highest values in the family.¹⁵ Recently, work from Maekawa et al.,¹⁶ reported a measurement of the ionic conductivity of Li_2ZnI_4 , where the authors reported low ionic conductivity (in the order of 1×10^{-6} S/cm) at 300 K. The material is an insulator, given that our computed HSE bandgap for this material is 4.28 eV. The estimated diffusion barrier of this material is 0.48 eV.

The pristine structure decomposes into the following products exothermically, indicating the metastability of the structure:



Such a structure would be stabilised by entropy as is the case in LGPS. At the lithium metal anode, Li_2ZnI_4 suffers from rapid decomposition into LiI and LiZn:



Decomposition of Li_2ZnI_4 at the lithium metal anode is less probable than that of LGPS, given that the crystal decomposition of LGPS is lower in energy, which is -646 meV/atom (Section S2 of the Supplementary Information).

LiGaI₃ (mp-29345): This lithium gallium halide is a stable phase (0 meV/atom energy above hull) and its synthesis and characterisation were first reported by Hoenle et al.¹⁷ A close neighbour of this compound, LiGaI₄, was identified by Kahle et al.⁶ as a very high diffusivity material, with a predicted $D_{1000\text{K}} > 1 \times 10^{-4}$ cm²/s and an activation barrier of 0.35 eV. However, to the best of our knowledge, LiGaI₃ was never suggested as an SSE material before. The diffusion barrier of this materials is 0.35 eV, which is greater than that of LGPS (0.19 eV¹⁸).

LiGaI₃ is strongly impacted by the presence of excess lithium ions at the anode interface:



This is similar to the behaviour of LiGaBr₃ for which the decomposition energy is -962 meV/atom, and indication that lithium halides might have large lithium conductivities at the expense of the structural integrity at the lithium metal interface.

LiInI₄ (mp-541001): This lithium indium halide exhibits a monoclinic P2₁/c space group and was first synthesized and characterised by Burnus and Meyer et al.¹⁹ Its ionic conductivity was experimentally examined by Yamada et al.²⁰ and found to exhibit low ionic conductivity (order of 1×10^{-8} S/cm). It was identified by Muy et al.²¹ as a potential SSE material. Their high-throughput screening was based on descriptors that predicted the phonon modes of the 14k Li-containing materials, and also identified by Ahmad et al.²² as a candidate SSE that might inhibit Li dendrite formation. The repeated appearance of this particular material in high-throughput screening works, while its measured conductivity is very small, and the fact that its computed diffusion barrier is 0.29 eV, should motivate further experimental measurements of its lithium conductivity.

However, this material is predicted to decompose into Li₃In and LiI at the lithium metal interface:



LiGaBr₄ (mp-28326): The structure of this lithium indium iodide is very similar to that of LiInI₄ and is also a stable phase. Its synthesis was first reported by Honle and Simon in 1986²³ and a related stoichiometry LiGaBr₃ was identified by Kahle et al. as a high conductivity material. However, Tomita et al.²⁴ have a measured high diffusion barrier of 0.37 eV, which is higher than the value estimated in this work, 0.22 eV. The room temperature lithium conductivity reported in the same reference is 7×10^{-6} S/cm, which is two-orders of magnitude higher than that of the related halide LiInI₄. The material was also identified by Gao et al.²⁵ as a candidate SSE material based on screening lithium bromide materials, who synthesised the material and reported a conductivity of 1×10^{-5} S/cm and a diffusion barrier of 0.51 eV. The difference in conductivity results from those reported in Ref.²³ is due to the different synthesis method.

In spite of its conductivity merits, this material is predicted to strongly decompose at the lithium metal interface into LiBr and LiGa:



Li₃YBr₆ (mp-1147619): This wide-gap bromide exhibits a monoclinic C2/c space group, and has an energy above the convex hull of 26 meV/atom, which indicates that it can potentially be synthesised in a stable phase. The family of halides Li₃MX₆ (M = Y, Er, X = Cl, Br, I) has recently gained intense interest owing to their high conductivity.^{26,27} Schlem et al.²⁶ have synthesised Li₃YBr₆ and Li₃YCl₆ and reported room temperature conductivities in the orders of 1×10^{-3} S/cm and 1×10^{-4} S/cm, respectively. Yu et al.²⁷ reported an ionic conductivity in the order of 1×10^{-3} S/cm for Li₃YBr₆, in addition to strategies to improve cathode-SSE interface stability. The material has not been identified in any of the high-throughput screening works Ref.^{5,6,22}.



The predicted diffusion barrier is low: 0.23 eV, while the R^2 for the Arrhenius plot fit is relatively high ($R^2 = 0.83$, see Figure 2e).

The decomposition of this material at the lithium metal interface makes it the next-most stable material after LLZP, and of special interest for the current work:



Li₂Mn₃Si₄O₈ (mp-849556): This hypothetical structure has a relatively high energy above the convex hull (52 meV/atom). The value of log($D_{1000\text{K}}$) is -4.4, and hence is comparable to that of LGPS. It has a low diffusion barrier of 0.15 eV in comparison with that of LGPS. However, this material is predicted to readily decompose at the interface with the lithium metal anode according to the following equation:



Li₂MnF₄ (mp-777589): This hypothetical lithium magnesium fluoride exhibits a tetragonal with the P4₃2₂ space group, and a low energy above the convex hull of 21 meV/atom, indicating the possibility of synthesis and phase stabilisation. The structure has not appeared in the material research literature. It has a low diffusion barrier of 0.10 eV, but is predicted to decompose readily at the anode interface:



The above analysis re-introduces Li_3YBr_6 as a candidate SSE based on its potential interface stability. Moreover, we emphasise that previously identified high conductivity materials, particularly LiGaI_4 and LiGaBr_3 , are also expected to rapidly decompose at the lithium metal surface based on the calculation of the interfacial decomposition energy. Next, we examine the defect thermodynamics of Li_3YBr_6 and the impact of defects on its lithium conductivity.

3.2 Detailed analysis: a potentially new SSE with planar conductivity

Li_3YBr_6 is the only entry in the Li-Y-Br chemical space in the MP database. However, the AFLOW²⁸ library hosts 94 hypothetical structures within this chemical space with formulas different from Li_3YBr_6 , all of which have higher formation energies, and hence are predicted to be less stable, than Li_3YBr_6 . The material has a layered structure in which layers of $\text{Li}_4\text{Y}_2\text{Br}_{12}$ are intercalated with Li atoms, hinting that the diffusion in this structure is two dimensional. By calculating the direction-resolved diffusion coefficients, in which we separate the planar (xy) diffusion from out-of-plane (z) diffusion, we find that the structure indeed favours a two-dimensional lithium conductivity, as can be seen in Figure 3a: the diffusion within the xy -plane is higher than that along the z -axis. The planar ordering of the Br atoms is nearly preserved during diffusion, even at high temperatures (900 K), as is shown in Figure 3b.

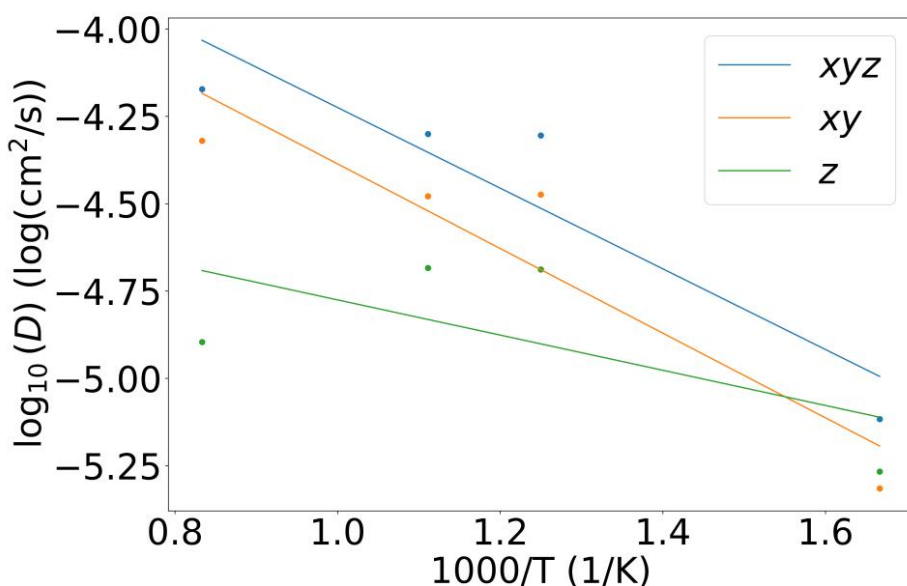
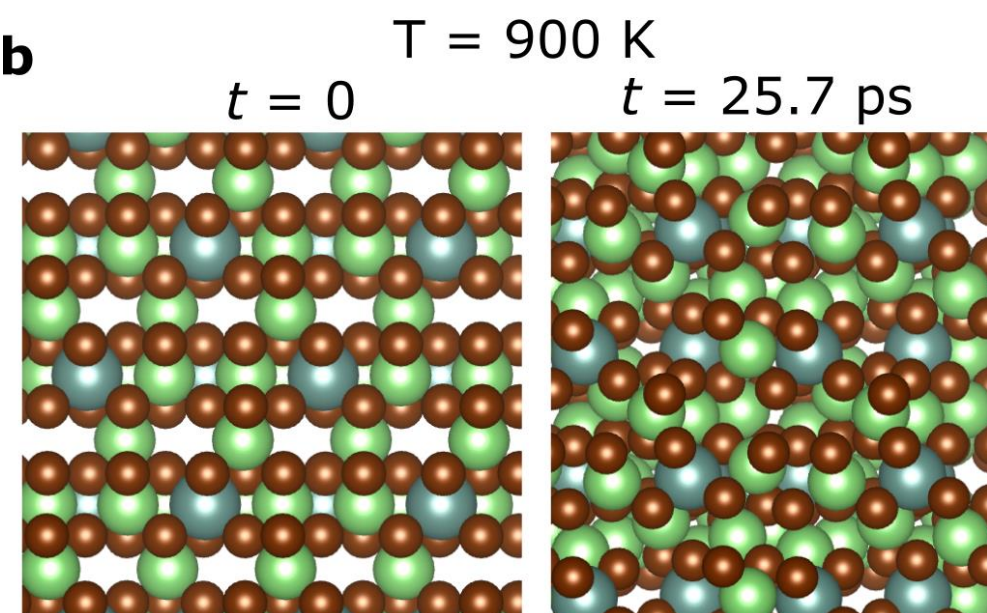
a**b**

Figure 3: (a) Resolution of the diffusion coefficients of Li_3YBr_6 into planar (xy) and perpendicular (z) components. (b) The atomic structure of a Li_3YBr_6 supercell before the simulation starts ($t = 0$) and after 25.7 ps, showing the characteristic Br layered structure is nearly preserved. Green spheres represent Li; blue for Y; brown for Br.

The planar structure of Li_3YBr_6 indicates that certain types of defects might impact the diffusivity of Li within the layers, as well as the structural integrity of the material.^{18,29,30} Defects where the planar Li atoms are removed or replaced with other atoms will negatively impact the planar conductivity of the material. We examine the native defects of Li_3YBr_6 by calculating the formation energies of its native defects via DFT calculations based on a 40-atom supercell. We apply the python package pymatgen-analysis-defects to enumerate the possible defect structures in Li_3YBr_6 , and we use the function

`add_interstitial()` from the `oganesson` python package to generate the interstitial defect. We then optimise all the defect supercells using DFT. The defects examined are interstitial Li defect Li_i^+ , the anti-site defects $\text{Br}_{\text{Li}}^{2-}$, $\text{Br}_{\text{Y}}^{4-}$, $\text{Li}_{\text{Br}}^{2+}$, $\text{Li}_{\text{Y}}^{2-}$, $\text{Y}_{\text{Br}}^{4+}$, $\text{Y}_{\text{Li}}^{2+}$, and the vacancy defects V_{Br}^+ , V_{Li}^- and V_{Y}^{3-} (where we use the convention that A_B means A replaces B). We display the formation energy profiles for these defects in Figure 4.

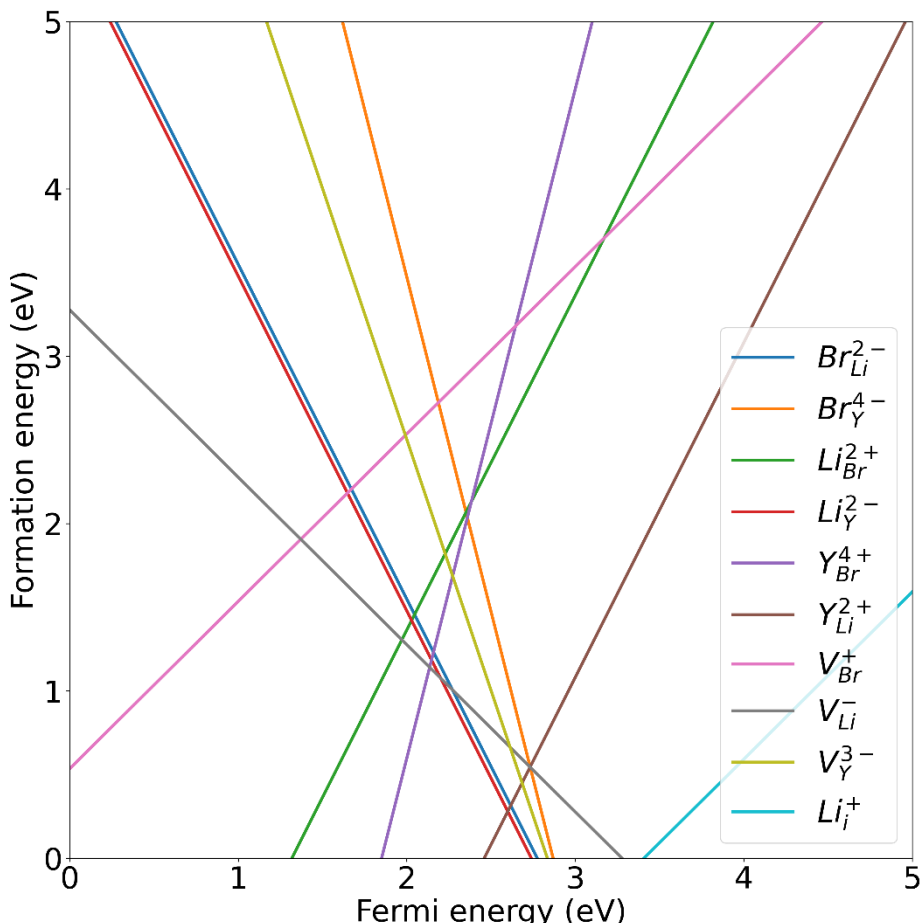


Figure 4: The defect formation energy profiles for the native defects in Li_3YBr_6 . The valence band maximum is set at 0.

Figure 4 shows that the material can host a broad range of co-existing native defects, except for the V_{Br}^+ defect (the pink line in Figure 4), for which the formation energy is larger than ~ 0.5 eV throughout the Fermi energy range. Observing the high cost of inducing a V_{Br}^+ defect corroborates with the near-integrity of the Br planes during the simulations, as displayed in Figure 3b. The defects that are most probably detrimental to the flow of lithium are the path blocking defects $\text{Br}_{\text{Li}}^{2-}$, $\text{Y}_{\text{Li}}^{2+}$, and the vacancy defect V_{Li}^- . Near the midgap (at Fermi energy within 2–3 eV) we find that these defects have negative formation energies, which means that they can form spontaneously.

We then examine the impact of the Li_3YBr_6 native defects on the conductivity of lithium by using the DIEP potential model³¹ using a $4 \times 4 \times 4$ supercell, with 2,560 atoms in total. The duration of each of the simulations is 50 ps. Simulating such a large supercell for a long time period cannot be feasibly afforded by present day supercomputing facilities. We label the AIMD-calculated diffusion coefficient values as triangles in Figure 5 for comparison with the DIEP-computed values. Even though this model over-estimates the diffusion coefficients by nearly an order of magnitude, the results of the model can offer an indication for changes in

the trend of the diffusion coefficients in defective systems, with respect to the diffusion in the pristine structure. We present in Figure 5 the diffusivity obtained for every defect configuration within the supercell, not only the defects with lowest formation energies (hence the multiple lines with the same colour). Substituting Br with Y ($\text{Y}_{\text{Br}}^{4+}$) and removing a Br atom (V_{Br}^+) are the defects with the most significant boost for the diffusion coefficients: they lead to a reduction in the diffusion activation energy by ~92% while increasing the low temperature diffusion coefficients. Given that $\text{Y}_{\text{Br}}^{4+}$ is energetically favourable according (see Figure 4), the material can be highly conductive at room temperature.

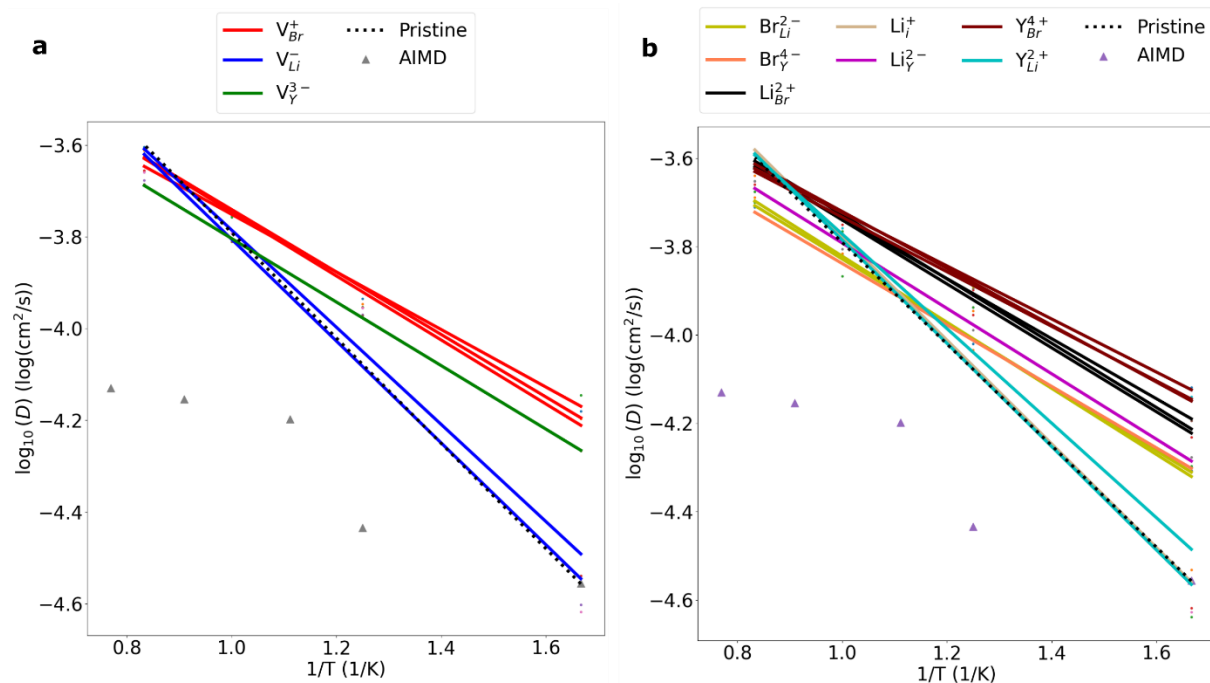


Figure 5: Simulation of the impact of native defects on the diffusivity of Li_3YBr_6 . Molecular dynamics simulations are performed using the DIEP machine learning potential model. We group the (a) vacancy defects and the (b) rest of the defects separately. The AIMD-computed diffusion coefficients for the pristine structure are displayed as triangles, for comparison.

Defects where Li replaces Br ($\text{Li}_{\text{Br}}^{2+}$) or Y (Li_Y^{2-}) also enhance the diffusion by reducing the activation energy. The presence of an interstitial Li (Li_i^+) has nearly no impact on diffusion because the position of the interstitial Li is in the gap between the two layers, and therefore this Li does not experience a concentration gradient from neighbouring Li atoms.

Thus, our BO approach has enabled us to identify a number of candidate SSE materials, including the new Li_3YBr_6 structure, from a search space set of 4.2k possible SSE materials by pointing us to only 1% of the search space. With the mean structure size is 41 atoms in the search space, for which we duplicate the supercell to 82 atoms, the computation of 40,000 simulation steps on 96 CPU cores requires ~490 hours, or 47k CPU-hours. The total amount of CPU-hours required for the entire search space is then ~200m CPU-hours, which is indeed a massive amount of computational resources. BO saved nearly 99% of this estimated cost, illustrating its value in experiment design.

4. Conclusion

As more car manufacturers head towards the commercialisation of solid state batteries, efficient computational approaches that combine artificial intelligence and material science must be sought to navigate the highly complex space of possible solid state electrolyte materials. This work applied Bayesian optimisation with *ab initio* molecular dynamics to search for potential candidate solid state electrolytes in a dataset of 4.2k materials, eventually leading to the selection of 7 materials after simulating the lithium diffusivity of 38 materials that were suggested by the Bayesian optimisation algorithm. We further scrutinised the thermodynamic stabilities of these 7 materials and identified Li₃YBr₆ as the least prone to interfacial decomposition.

Acknowledgements

S. A. T. recognizes the support of the Alfred Deakin Postdoctoral Research Fellowship from Deakin University. This work was supported by computational resources provided by the Australian Government through the National Computational Infrastructure National Facility and the Pawsey Supercomputer Centre.

References

- (1) *Electric Vehicles*, <Https://Www.Iea.Org/Reports/Electric-Vehicles>; 2022. <https://www.iea.org/reports/electric-vehicles>.
- (2) Pasta, M.; Armstrong, D.; Brown, Z. L.; Bu, J.; Castell, M. R.; Chen, P.; Cocks, A.; Corr, S. A.; Cussen, E. J.; Darnbrough, E.; Deshpande, V.; Doerrer, C.; Dyer, M. S.; El-Shinawi, H.; Fleck, N.; Grant, P.; Gregory, G. L.; Grovenor, C.; Hardwick, L. J.; Irvine, J. T. S.; Lee, H. J.; Li, G.; Liberti, E.; McClelland, I.; Monroe, C.; Nellist, P. D.; Shearing, P. R.; Shoko, E.; Song, W.; Jolly, D. S.; Thomas, C. I.; Turrell, S. J.; Vestli, M.; Williams, C. K.; Zhou, Y.; Bruce, P. G. 2020 Roadmap on Solid-State Batteries. *J. Phys. Energy* **2020**, 2 (3), 032008. <https://doi.org/10.1088/2515-7655/ab95f4>.
- (3) Solid Power, Backed by Ford and BMW, Begins Pilot Production of Innovative EV Battery with Longer Range and Quicker Recharging. June 6, 2022. <https://www.cnbc.com/2022/06/06/solid-power-begins-pilot-production-of-solid-state-ev-battery.html>.
- (4) Urban, A.; Seo, D.-H.; Ceder, G. Computational Understanding of Li-Ion Batteries. *Npj Comput. Mater.* **2016**, 2 (1), 16002. <https://doi.org/10.1038/npjcompumats.2016.2>.
- (5) Sendek, A. D.; Yang, Q.; Cubuk, E. D.; Duerloo, K.-A. N.; Cui, Y.; Reed, E. J. Holistic Computational Structure Screening of More than 12 000 Candidates for Solid Lithium-Ion Conductor Materials. *Energy Environ. Sci.* **2017**, 10 (1), 306–320. <https://doi.org/10.1039/C6EE02697D>.
- (6) Kahle, L.; Marcolongo, A.; Marzari, N. High-Throughput Computational Screening for Solid-State Li-Ion Conductors. *Energy Environ. Sci.* **2020**, 13 (3), 928–948. <https://doi.org/10.1039/C9EE02457C>.
- (7) Ling, C. A Review of the Recent Progress in Battery Informatics. *Npj Comput. Mater.* **2022**, 8 (1), 33. <https://doi.org/10.1038/s41524-022-00713-x>.
- (8) Brochu, E.; Cora, V. M.; de Freitas, N. A Tutorial on Bayesian Optimization of Expensive Cost Functions, with Application to Active User Modeling and Hierarchical Reinforcement Learning. **2010**. <https://doi.org/10.48550/ARXIV.1012.2599>.
- (9) Ryan, S.; Berk, J.; Rana, S.; McDonald, B.; Venkatesh, S. A Bayesian Optimisation Methodology for the Inverse Derivation of Viscoplasticity Model Constants in High Strain-Rate Simulations. *Def. Technol.* **2022**, 18 (9), 1563–1577. <https://doi.org/10.1016/j.dt.2021.10.013>.

- (10) Frazier, P. I.; Wang, J. Bayesian Optimization for Materials Design. In *Information Science for Materials Discovery and Design*; Lookman, T., Alexander, F. J., Rajan, K., Eds.; Springer Series in Materials Science; Springer International Publishing: Cham, 2016; Vol. 225, pp 45–75. https://doi.org/10.1007/978-3-319-23871-5_3.
- (11) Jain, A.; Ong, S. P.; Hautier, G.; Chen, W.; Richards, W. D.; Dacek, S.; Cholia, S.; Gunter, D.; Skinner, D.; Ceder, G.; Persson, K. A. Commentary: The Materials Project: A Materials Genome Approach to Accelerating Materials Innovation. *APL Mater.* **2013**, *1* (1), 011002. <https://doi.org/10.1063/1.4812323>.
- (12) Wenzel, S.; Randau, S.; Leichtweiß, T.; Weber, D. A.; Sann, J.; Zeier, W. G.; Janek, J. Direct Observation of the Interfacial Instability of the Fast Ionic Conductor Li₁₀GeP₂S₁₂ at the Lithium Metal Anode. *Chem. Mater.* **2016**, *28* (7), 2400–2407. <https://doi.org/10.1021/acs.chemmater.6b00610>.
- (13) Zhu, Y.; He, X.; Mo, Y. Origin of Outstanding Stability in the Lithium Solid Electrolyte Materials: Insights from Thermodynamic Analyses Based on First-Principles Calculations. *ACS Appl. Mater. Interfaces* **2015**, *7* (42), 23685–23693. <https://doi.org/10.1021/acsami.5b07517>.
- (14) Pfitzner, A.; Lutz, H. D.; Cockcroft, J. K. Li₂ZnI₄: A Neutron Powder Study. *J. Solid State Chem.* **1990**, *87* (2), 463–466. [https://doi.org/10.1016/0022-4596\(90\)90050-8](https://doi.org/10.1016/0022-4596(90)90050-8).
- (15) Lutz, H. D.; Wussow, K.; Kuske, P. Ionic Conductivity, Structural, IR and Raman Spectroscopic Data of Olivine, Sr₂PbO₄, and Na₂CuF₄ Type Lithium and Sodium Chlorides Li₂ZnCl₄ and Na₂Mg₂Cl₄ (M = Mg, Ti, Cr, Mn, Co, Zn, Cd). *Solid State Ion.* **2008**, *178* (31–32), 1637–1641. <https://doi.org/10.1016/j.ssi.2007.10.018>.
- (16) Höhne, W.; Miller, G.; Simon, A. Preparation, Crystal Structures, and Electronic Properties of LiGaCl₃ and LiGaI₃. *J. Solid State Chem.* **1988**, *75* (1), 147–155. [https://doi.org/10.1016/0022-4596\(88\)90312-X](https://doi.org/10.1016/0022-4596(88)90312-X).
- (17) Oh, K.; Chang, D.; Lee, B.; Kim, D.-H.; Yoon, G.; Park, I.; Kim, B.; Kang, K. Native Defects in Li₁₀GeP₂S₁₂ and Their Effect on Lithium Diffusion. *Chem. Mater.* **2018**, *30* (15), 4995–5004. <https://doi.org/10.1021/acs.chemmater.8b01163>.
- (18) Burnus, R.; Meyer, G. Synthese Und Kristallstrukturen Der Alkali-Tetraiodoindate(III), AlnI₄ (A = Li, K, Rb, Cs). *Z. Für Anorg. Allg. Chem.* **1991**, *602* (1), 31–37. <https://doi.org/10.1002/zaac.19916020104>.
- (19) Yamada, K.; Matsuyama, S.; Tomita, Y.; Yamane, Y. Lithium Ion Conduction Mechanism in LiInI₄ Studied by Single Crystal ⁷Li NMR. *Solid State Ion.* **2011**, *189* (1), 7–12. <https://doi.org/10.1016/j.ssi.2011.02.020>.
- (20) Muy, S.; Voss, J.; Schlem, R.; Koerver, R.; Sedlmaier, S. J.; Maglia, F.; Lamp, P.; Zeier, W. G.; Shao-Horn, Y. High-Throughput Screening of Solid-State Li-Ion Conductors Using Lattice-Dynamics Descriptors. *iScience* **2019**, *16*, 270–282. <https://doi.org/10.1016/j.isci.2019.05.036>.
- (21) Ahmad, Z.; Xie, T.; Maheshwari, C.; Grossman, J. C.; Viswanathan, V. Machine Learning Enabled Computational Screening of Inorganic Solid Electrolytes for Suppression of Dendrite Formation in Lithium Metal Anodes. *ACS Cent. Sci.* **2018**, *4* (8), 996–1006. <https://doi.org/10.1021/acscentsci.8b00229>.
- (22) Hoenle, W.; Simon, A. Darstellung Und Kristallstrukturen von Li₂GaBr₄ Und Li₂GaBr₃. *Z. Fuer Naturforschung Teil B Anorg. Chem. Org. Chem.* **1986**, *41*, 1391–1398.

- (24) Tomita, Y. Ionic Conductivity and Structure of Halocomplex Salts of Group 13 Elements. *Solid State Ion.* **2000**, 136–137 (1–2), 351–355. [https://doi.org/10.1016/S0167-2738\(00\)00491-4](https://doi.org/10.1016/S0167-2738(00)00491-4).
- (25) Gao, L.; Zhong, F.; Tong, Y.; Zhang, S.; You, J.; Wei, H.; Yu, X.; Xu, S.; Zhao, G. High Formability Bromide Solid Electrolyte with Improved Ionic Conductivity for Bulk-Type All-Solid-State Lithium–Metal Batteries. *ACS Appl. Energy Mater.* **2022**, 5 (9), 10604–10610. <https://doi.org/10.1021/acs.chemmater.2c01343>.
- (26) Schlem, R.; Banik, A.; Ohno, S.; Suard, E.; Zeier, W. G. Insights into the Lithium Sub-Structure of Superionic Conductors Li_3YCl_6 and Li_3YBr_6 . *Chem. Mater.* **2021**, 33 (1), 327–337. <https://doi.org/10.1021/acs.chemmater.0c04352>.
- (27) Yu, C.; Li, Y.; Adair, K. R.; Li, W.; Goubitz, K.; Zhao, Y.; Willans, M. J.; Thijs, M. A.; Wang, C.; Zhao, F.; Sun, Q.; Deng, S.; Liang, J.; Li, X.; Li, R.; Sham, T.-K.; Huang, H.; Lu, S.; Zhao, S.; Zhang, L.; Van Eijck, L.; Huang, Y.; Sun, X. Tuning Ionic Conductivity and Electrode Compatibility of Li_3YBr_6 for High-Performance All Solid-State Li Batteries. *Nano Energy* **2020**, 77, 105097. <https://doi.org/10.1016/j.nanoen.2020.105097>.
- (28) Curtarolo, S.; Setyawan, W.; Wang, S.; Xue, J.; Yang, K.; Taylor, R. H.; Nelson, L. J.; Hart, G. L. W.; Sanvito, S.; Buongiorno-Nardelli, M.; Mingo, N.; Levy, O. AFLOWLIB.ORG: A Distributed Materials Properties Repository from High-Throughput Ab Initio Calculations. *Comput. Mater. Sci.* **2012**, 58, 227–235. <https://doi.org/10.1016/j.commatsci.2012.02.002>.
- (29) Squires, A. G.; Scanlon, D. O.; Morgan, B. J. Native Defects and Their Doping Response in the Lithium Solid Electrolyte $\text{Li}_7\text{La}_3\text{Zr}_2\text{O}_{12}$. *Chem. Mater.* **2020**, 32 (5), 1876–1886. <https://doi.org/10.1021/acs.chemmater.9b04319>.
- (30) Hoang, K.; Johannes, M. D. Defect Chemistry in Layered Transition-Metal Oxides from Screened Hybrid Density Functional Calculations. *J Mater Chem A* **2014**, 2 (15), 5224–5235. <https://doi.org/10.1039/C4TA00673A>.
- (31) Tawfik, S. A.; Nguyen, T. M.; Russo, S. P.; Tran, T.; Gupta, S.; Venkatesh, S. Enabling Discovery of Materials through Enhanced Generalisability of Deep Learning Models. arXiv April 30, 2024. <http://arxiv.org/abs/2402.10931> (accessed 2024-06-05).